

A comprehensive sintering mechanism for TBCs-Part II: Multiscale multipoint interconnection-enhanced initial kinetics

Guangrong Li | Hua Xie | Guanjun Yang  | Gang Liu | Chengxin Li | Changjiu Li

State Key Laboratory for Mechanical Behavior of Materials, School of Materials Science and Engineering, Xi'an Jiaotong University, Xi'an, Shaanxi Province, China

Correspondence

Guanjun Yang, State Key Laboratory for Mechanical Behavior of Materials, School of Materials Science and Engineering, Xi'an Jiaotong University, Xi'an, Shaanxi, China.
Email: ygj@mail.xjtu.edu.cn

Funding information

National Basic Research Program of China, Grant/Award Number: No. 2013CB035701; Fundamental Research Funds for the Central Universities; National Program for Support of Top-notch Young Professionals

Abstract

During thermal exposure, the sintering process of the plasma-sprayed thermal barrier coatings (PS-TBCs) presents significant two-stage kinetics, as reported in the Part I. As a companion study, this part aims to reveal the mechanism responsible for the ultrafast sintering kinetics when initially exposed, since the initial short stage (stage-I) often finishes most increment of the mechanical and thermal properties. A detailed examination of the pore healing behavior was carried out, based on the experimental result in Part I that the dominant structural change at the stage-I is the significant healing at intersplat pore tips. Results show that the smooth splat surface, which made up the wedge-shaped intersplat pores, changed to a rough surface with multiscale convexs after high-temperature thermal exposure. Moreover, the multiscale roughening is highly sensitive to various orientations of the columnar grains inside the splats. Subsequently, multipoint connection between the counter-surfaces of the intersplat pores was formed by the bridging of multiscale convexs. This multiscale multipoint connection between pore surfaces significantly accelerated the healing of intersplat pores, which can be dominantly responsible for the ultrafast sintering kinetics at the stage-I. This comprehensive sintering mechanism could offer some positive suggestions toward prolonging the thermal-insulating effect of TBCs.

KEYWORDS

lamellar structure, multiconnection, sintering, thermal barrier coatings, ultrahigh temperature

1 | INTRODUCTION

Plasma-sprayed yttria-stabilized zirconia (PS-YSZ) continues to dominate the thermal-insulating application of thermal barrier coatings (TBCs), which are widely used in both aero- and land-based gas turbine engines.^{1–3} Two highly concentrated performances of the TBCs are the thermal barrier effect and the durability exposed to high temperatures, both of which depend closely on the unique microstructure of the PS-YSZ.

The PS-YSZ coatings is formed by successive deposition of a stream of fully molten or partially molten particles impacting on a substrate followed by lateral flattening,

rapid solidification and cooling from a temperature over the melting point.⁴ As a result, the coating exhibits a lamellar structure.⁵ The lamellae are formed with columnar grains oriented along the heat flow by and large.⁶ It is widely accepted that the excellent performances of PS-YSZ coatings is primarily attributed to the pore-rich microstructure comprising intersplat pores and intrasplat cracks.^{5,7} The intersplat pores generally correspond to the imperfect bonding between splats. That is why the plasma-sprayed ceramic coatings present approximately 30% bonding ratio between layers without preheating on substrate.⁵ The intrasplat cracks are generated during the splat quenching to relieve thermal stress.^{8,9} Consequently, this pore-rich

structure contributes to $>1/2$ drop of both the through-thickness thermal conductivity^{3,10} and the in-plane Young's modulus^{11–13} with respect to those of the bulk YSZ.

However, during thermal exposure, sintering leads to significant healing of these pores, which has an increasingly detrimental effect on the performances of TBCs. In Part I,¹⁴ the overall sintering process of the PS-YSZ coatings is divided into two stages approximately, i.e., an ultrafast kinetics at the initial short stage (stage-I) and a much slower kinetics at the following thermal exposure duration (stage-II). At the stage-I, the ultrafast sintering kinetics is primarily attributed to the rapid healing of intersplat pore tips. It is worth noting that, in spite of a short duration, the stage-I finishes a vast majority of the whole sintering. For example, the initial 10 hours thermal exposure at 1350°C resulted in a shrinkage of 0.7% with respect to that of 1.4% during the whole 150 hours thermal exposure.¹⁵ Therefore, the sintering mechanism, in particular, at the stage-I, is essential to understand the structure/properties evolution of PS-YSZ coatings.

According to that observed in conventional ceramic sintering or described in powder metallurgy theories, the sintering process begins with the connection of particles, and a neck is formed to transport materials and promote the diffusion of elements and defects.¹⁶ The whole process is accompanied with the increase of the neck diameter and the shrinkage of pores. Except for the existing touching area formed during precompaction, there is almost no other newly formed connecting point. Moreover, the particles do not show any orientations from an overall view, since they are randomly distributed. Therefore, the microstructure of powder materials is usually assumed to be isotropic. However, this assumption is not applicable to the splat-stacked coating, since the properties (like thermal conductivity¹⁷ and elastic modulus¹⁸) in the in-plane direction of the coating are much different from those in the out-plane direction. To sum up, the unique microstructure determines that the sintering of PS-YSZ coatings does make a distinction, comparing to the sintering of powder-metallurgic materials. With the microstructural characterization by transmission electron microscopy, the formation of some new connecting points between lamellar splats is observed, which is possible the main reason responsible for the increase of properties.^{19,20}

The unique pores structure, as well as the special grain orientation, of PS-YSZ coatings suggests that a comprehensive consideration of both the intrinsic material behavior and the structural evolution is highly necessary. Some papers investigated the sintering behavior of PS-YSZ coatings by revealing their intrinsic sintering behavior of materials, in particular, like the temperature-dependent grain growth rates²¹ and the various dominant diffusion mechanisms at different temperatures.²² However, it is still not

well understood owing to the fact that the sintering behavior of PS-YSZ coatings is material and structure specific. Toward this orientation, Cipitria et al.⁹ proposed a systematic sintering model, in which the following three assumptions were made without carefully correlating to the experiments, i.e. equally thick pore architecture, smooth pore surface morphology and one-dimensional pore boundary healing mode. The sintering process only during the relatively long duration seems quantitatively understood based on this model.⁹ Unfortunately, the model prediction cannot be well consistent with the ultrafast sintering kinetics during the early stage obtained by experiments.⁹ Even the bimodal size distribution of pore structure was further proposed and taken into consideration, the above-mentioned discrepancy cannot be well explained.⁹ Actually, few literatures have been focused on the ultrafast sintering kinetics during the early stage associated with the PS ceramic coatings. Therefore, it is highly necessary to understand the sintering behavior during the stage-I based on a comprehensive consideration of both the material and the microstructure of PS-YSZ coatings.

As a second part coherent to the two-stage sintering kinetics of PS-YSZ coatings, this study aims to reveal the ultrafast sintering kinetics at the stage-I. A detailed examination on the morphological changes of pore surface was carried out. Subsequently, the surface changes were correlated to the grain orientation. Finally, a multiconnection mechanism induced by the surface changes is proposed to account for the ultrafast sintering kinetics at the stage-I. With these experimental data, the comprehensive sintering mechanism for lamellar TBCs reported in Part I could be further enriched, which would benefit the structural tailoring of TBCs with enhanced thermal-insulating effects.

2 | EXPERIMENTAL PROCEDURE

2.1 | Materials and sample preparation

The PS-YSZ coating is formed in a layer-by-layer manner, as shown in Figure 1A. At the interface between top coat and bond coat, the first layer was partially bonded to the bond coat (the roughness of bond coat was neglected). Therefore, the unbonded area is the residual bottom area of splats in the first layer, as shown in Figure 1B(A). At any locations inside the coatings, the unbonded area is also the residual areas in neighboring two layers. It is obvious that these residual areas form the intersplat pores, as shown in Figure 1B(B). Therefore, it can be concluded that the surfaces of intersplat pores, despite of their locations in coatings, are actually either top surface or bottom surface of individual splats with columnar grains. The aim of this study was to investigate the healing behavior of these intersplat pores related to morphological changes of their pore

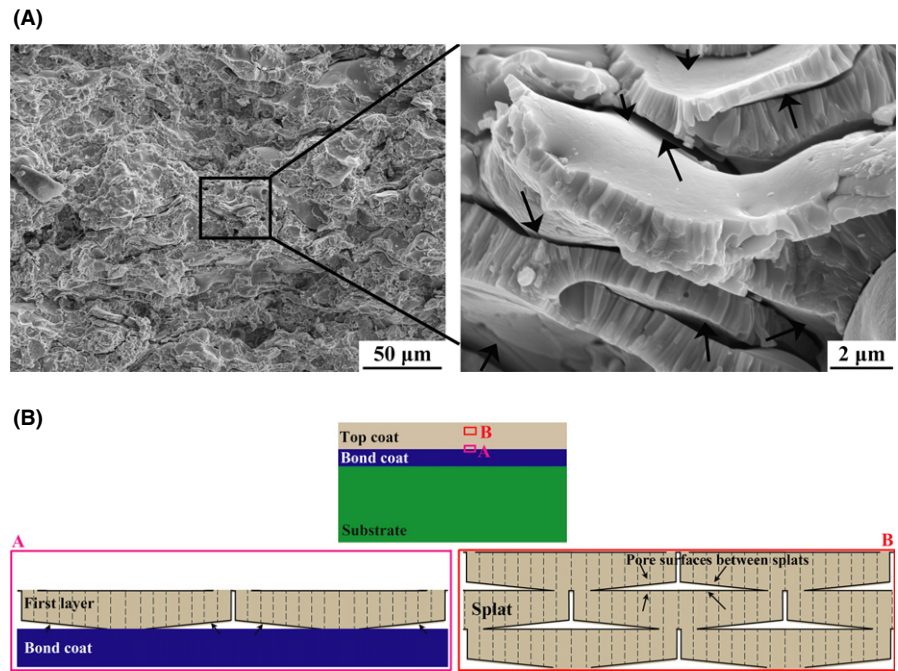


FIGURE 1 Cross section of the plasma-sprayed YSZ coatings: (A) lamellar structure with intersplat pores; (B) schematics to show the surfaces of intersplat pores at different locations of YSZ coatings. The black arrows refer to the pore surfaces

TABLE 1 Plasma spray parameters for individual splats and coatings

| Parameters | Individual splats | Coatings |
|---|-------------------|----------|
| Plasma arc voltage/V | 70 | 70 |
| Plasma arc current/A | 600 | 600 |
| Flow rate of primary gas (Ar)/L min ⁻¹ | 50 | 50 |
| Flow rate of secondary gas (H ₂)/L min ⁻¹ | 7 | 7 |
| Flow rate of powder feeding gas (N ₂)/L min ⁻¹ | 6 | 6 |
| Spray distance/mm | 110 | 110 |
| Torch traverse speed/mm s ⁻¹ | 1000 | 800 |
| Substrate preheating temperature (C) | 300 | / |

surface. However, it would be rather difficult to conduct this investigation based on YSZ coatings directly. To simplify this problem, the surface morphology of individual YSZ splats was used to serve as the intersplat pore surface.

A commercial fused-crushed 8 wt% YSZ powder (FC, 5–22 μm, Fujimi, Aichi, Japan) was used as feedstock. Oxidation would occur when a metal substrate is used during thermal test, and thus it may affect the observation of pore surface. Therefore, bulk YSZ substrate with polished surface was used to support the individual splats. The YSZ substrate was preheated to about 300°C to obtain disk-shaped individual splats. A pyrometer (RAYR312ML3U, Raytek, Santa Cruz, CA) was used to monitor the surface temperature during spraying. Other details of the preheating setup can be found elsewhere.⁴ In addition, similar to Part

I,¹⁴ YSZ coatings were prepared using a commercially available hollow spheroidized 8 wt% YSZ powder (HOSP, −75 to +45 μm, Metco 204B-NS, Sulzer Metco Inc., New York). Stainless steel was used as support for the coating deposition. Subsequently, the stainless steel was removed through postspray dissolution by hydrochloric acid, with the aim to obtain free-standing YSZ coatings. The plasma spray parameters for the individual splats and the coatings were shown in Table 1.

2.2 | Thermal exposure of samples

The combustion atmosphere under realistic conditions can be very harsh, including high pressures (up to 10 atm.), high temperature (up to 1400°C), high gas velocities, as well as the presence of detrimental environmental species (e.g., water vapor, sand, ash, salt).²³ All these present a big challenge on the function and the lifetime of TBCs. For instance, the particles carried by the combusted gas may lead to the spallation of TBCs.²⁴ The water vapor has been found to be a negative factor regarding the failure of TBCs.^{25,26} The high gas velocity may possibly accelerate the spallation of TBCs.²⁷ The degradation of TBCs induced by corrosion of molten deposits (e.g., CMAS being short for calcium-magnesium aluminosilicates) was also widely reported.^{28,29} In this study, a simplified atmosphere in air was considered, with the aim to focus on the intrinsic sintering behavior of TBCs during thermal exposure.

The working temperature for TBCs is approximately 1000°C, and the corresponding life time can be as long as 8000–16 000 hours. In order to accelerate the sintering

process, a higher temperature is necessary. Therefore, the samples were isothermally heat treated to temperatures of 1000°C and 1300°C. After progressively holding for different durations, the samples were cooled down to room temperature. The other details for the heat treatment can be found in Part I.¹⁴

Based on the results of the Part-I,¹⁴ the durations of stage I at 1000°C and 1300°C were approximately 50 hours and 10 hours, respectively. However, the significant formation of monoclinic phase often needs a much longer incubation period (e.g., 100-150 hours at 1300°C³⁰⁻³²). Therefore, it is reasonable to conclude that the sintering at stage I is relatively unaffected by the phase change.

2.3 | Characterization of YSZ deposits

An atomic force microscopy (AFM) system (Asylum Research Cypher, USA) was used to examine the surface morphology of individual splats. Figure 2 shows the schematics of AFM observation on an individual splat. Although the AFM has an acceptable vertical resolution, it is still hard to focus on a same domain before and after thermal exposure. Therefore, a pre-position determined by an optical microscopy was used to guarantee that the observation was carried out on the same domain of a same splat. Based on this method, repeated observations on the same splat after progressive thermal exposure durations were carried out to obtain statistical results.

Cross-sectional morphology of the YSZ coatings was examined using a scanning electron microscope (SEM) system (TESCAN MIRA 3, Czech). Similar to the examination of AFM, the quasi in situ morphological observation for intersplat pores was also examined using SEM.

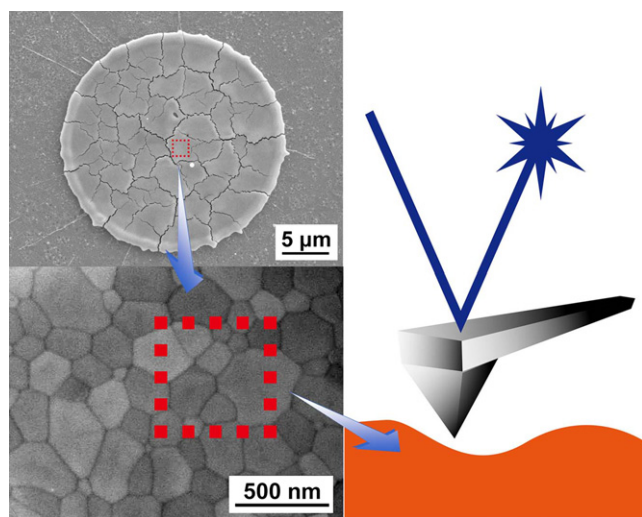


FIGURE 2 AFM examination of the surface of an individual splat

The detailed procedure for the quasi in situ observation can be found in the Part I and would also be described here. To begin with, a target position was found at a high magnification. Subsequently, the magnification decreased gradually until the whole sample could be observed. Meanwhile, the target position was fixed at this magnification by measuring its coordinates. After thermal exposure, the corresponding coordinates were used to find the target position. Regarding the polished cross section of the YSZ coatings before and after thermal exposure, the observations were conducted on different samples. It is highly necessary to preferentially infiltrate epoxy resin into the as-deposited coating and the exposed coatings. Subsequently, the samples can be polished and observed. Electron backscattered diffraction method (EBSD) was used to determine crystalline orientations of the columnar grains in splats.

3 | RESULTS

3.1 | Faceting of grain surface during thermal exposure

In this section, the scanning area of AFM was $1 \times 1 \mu\text{m}^2$, while the selected grain size is larger than $1 \mu\text{m}$ by and large. Therefore, the scanning revealed the information of one single grain. Figure 3 shows the surface changes after progressive thermal exposure. Before the thermal exposure, the surface of bared grain boundaries exhibited a relatively smooth morphology (marked as untreated in Figure 3). After 5 hours of thermal exposure at 1000°C (see Figure 3A), the surface within a grain tended to be wrinkle and facet. With the increase of the thermal exposure duration, the faceting phenomenon tended to be more significant with different concave and convex areas. Meanwhile, the variation of hills and valleys in height tended to grow. The peak wavelength was in a scale of approximately 10 nm. With the further increase of the thermal exposure duration, the faceting tended to be more remarkable, i.e., the peak height, as well as the size of faceting, presented an increasing trend. Moreover, it was found that a higher exposure temperature resulted in an increase in the intensity of faceting (see Figure 3B). The faceting effect can be explained essentially by the anisotropic-specific surface free energy. Morterra et al.³³ found that Y stabilized t-ZrO₂ appears to show small coin-like morphology with the (111) surface favored at a lower calcination temperature of approximately 600°C, and this morphology changes to pebble-like crystals with (101) as a dominant surface at a higher calcination temperature. Some recent studies proposed that the surface morphological changes might be more stable than some flat YSZ surface.³⁴⁻³⁶

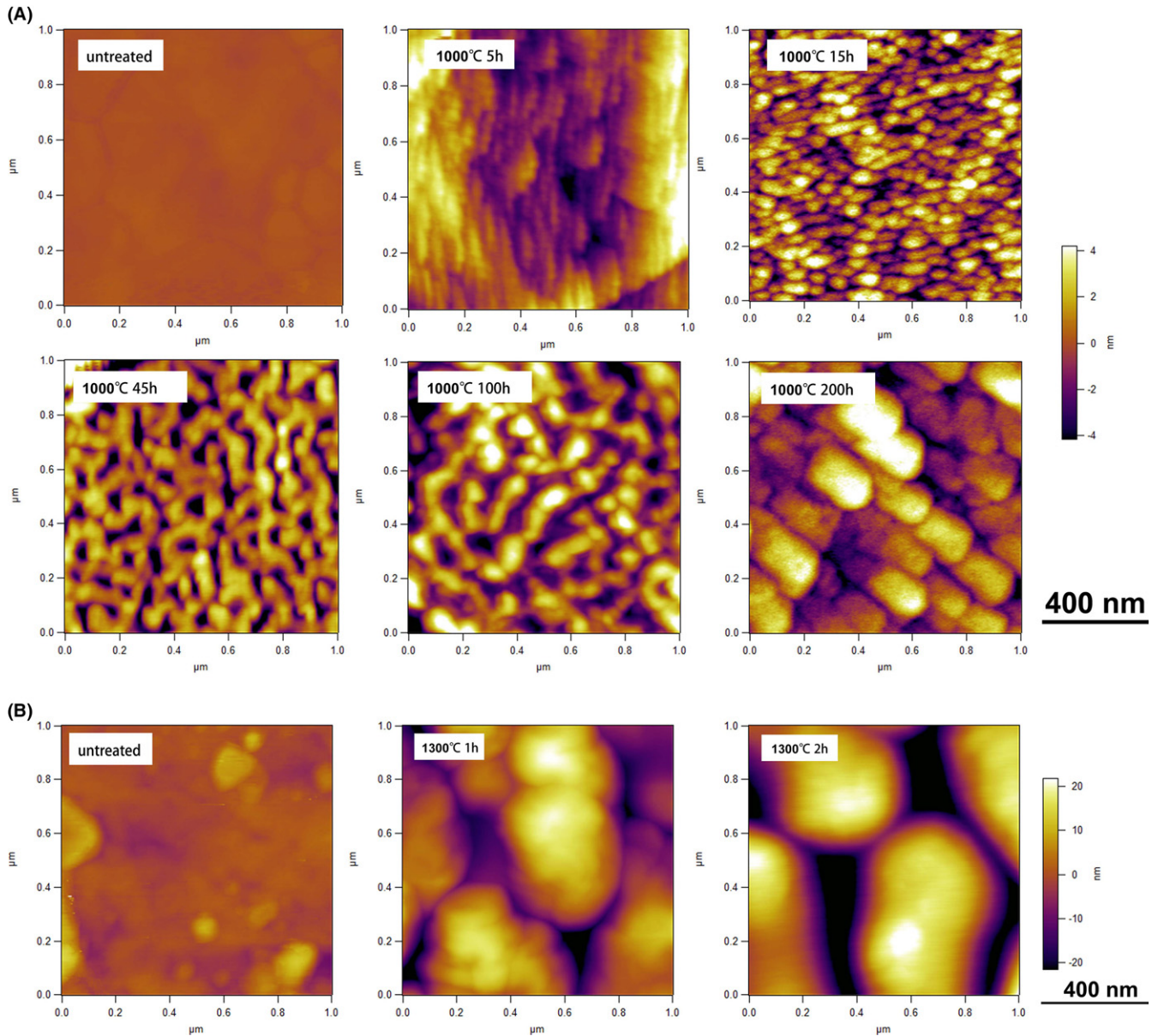


FIGURE 3 Morphological changes of an individual splat surface after thermal exposure at 1000°C (A) and 1300°C (B)

3.2 | Grooving of bared grain boundary during thermal exposure

In this section, the scanning area of AFM was $2.5 \times 2.5 \mu\text{m}^2$, while the selected grain size is approximately $1 \mu\text{m}$. Therefore, the scanning revealed the information of several grains, including their grain boundaries. Figure 4 shows the effect of thermal exposure on the bared surface of grain boundaries. It is possible to observe that, after thermal exposure, the profile of the surface evolved from an initially flat profile to a profile containing faceting thermal grooves, and finally, to a global step-like profile. During the faceting process, the edges of bared grain boundaries were much higher than the center of the same grain.

Even under a same thermal exposure condition, the rate of grooving and faceting in different grain boundaries are different. Figure 4A demonstrates this kind of divergence in different grain boundaries. It seems that the grooving and faceting rate are not affected by the size of columnar grains. Moreover, the faceting orientation of each grain presented an obvious distinction. Figure 4A also demonstrates the difference in columnar grain heights. In other words, different columnar grains presented different overall heights despite the same height before thermal exposure. Figure 5 shows the EBSD pattern of the splat surface before thermal exposure. Different colors in Figure 5 stand for different values of Euler angles. Therefore, each color represents a unique orientation of crystal lattice. The unresolved zones

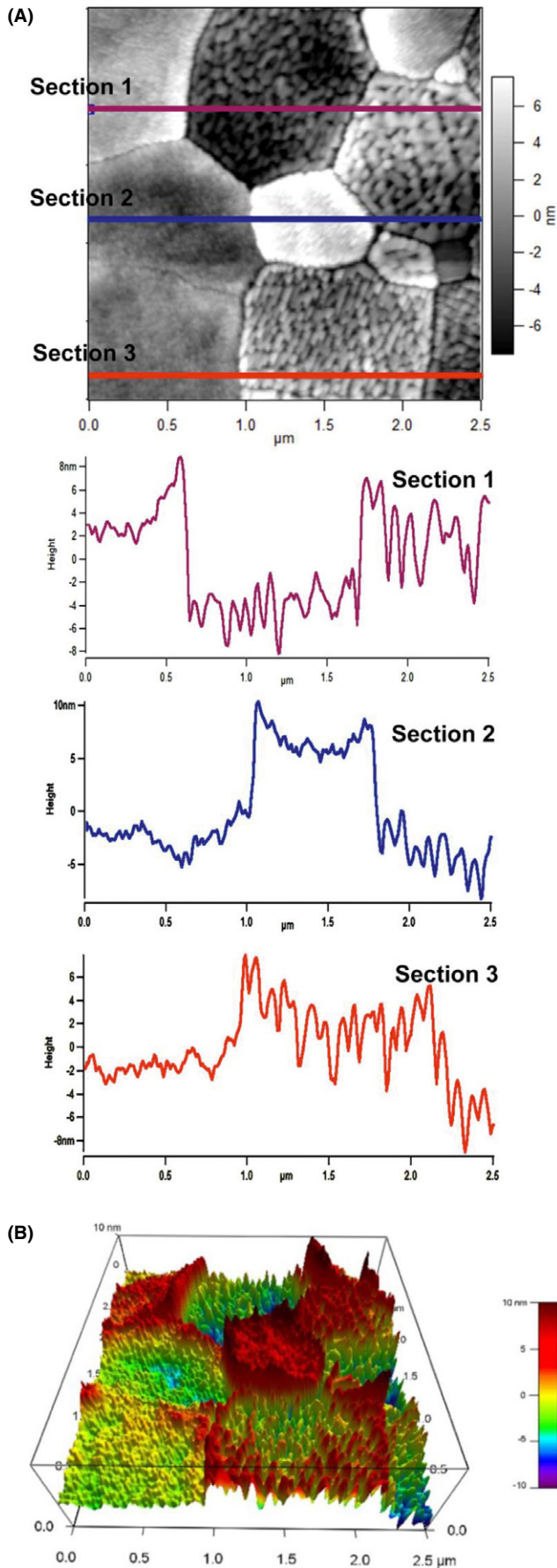


FIGURE 4 Divergence in grooving and faceting: (A) shows the measured surface profiles, which illustrate the convexes near grain boundaries and the grain-boundary grooving across the line marked with different colors after thermal exposure at 1000°C for 45 hours; and (B) a three-dimensional surface profile corresponding to (A)

in a black color represent the grain boundaries. However, the pole figure shows that there is no obvious texture, since the max value of multiples of unit distribution (MUD) is 5.01 (It is generally believed that there would be obvious preferred orientation when the Max MUD is larger than 10). In brief, each grain in the splat actually has a different lattice orientation from its neighboring grains, which may be the dominant reason responsible for the different rates of grooving and faceting.

3.3 | SEM investigation of sintering process

Figure 6 displays the morphological changes in counter-surfaces of the intersplat pores after progressive thermal exposure at 1300°C for 1, 5, and 10 hours. It can be observed that the localized surface of grains became roughened, which lead to a direct contact with adjacent grains. Figure 7 shows morphologies of the polished cross section of YSZ coatings before and after thermal exposure at 1300°C for 10 hours. The black lines in the cross sections refer to the intersplat pores and intrasplat cracks, and thus the two edges of the black lines correspond to the counter-surface of intersplat pores. Significant sintering occurred at the intersplat pores after thermal exposure. On the one hand, the counter-surfaces of intersplat pores at the as-deposited state were smooth. In contrast, after thermal exposure, the counter-surfaces tended to be roughening. On the other hand, the originally continuous pores were interrupted by forming bridges between counter-surfaces of the intersplat pores (see Figure 7B).

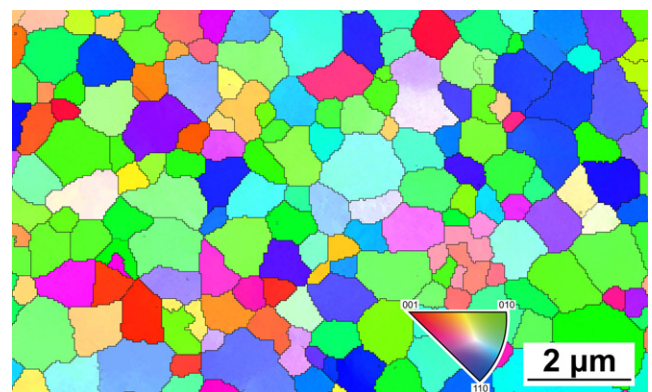


FIGURE 5 EBSD pattern of the grain surface of a splat

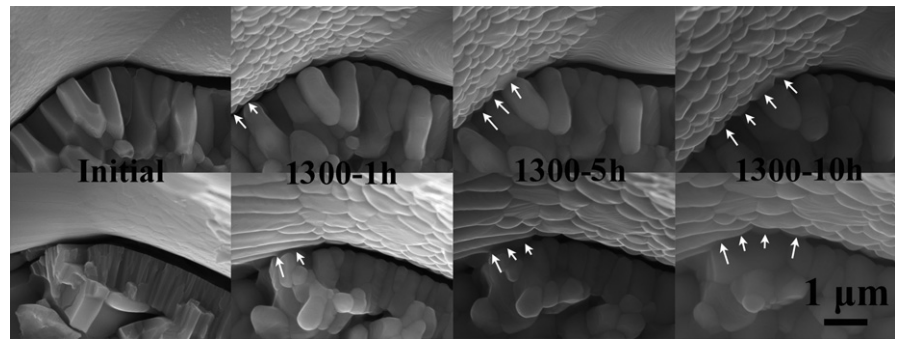


FIGURE 6 Quasi in situ morphological changes of counter-surfaces of the intersplat pores in a cross-sectioned YSZ coating thermally exposed at 1300°C

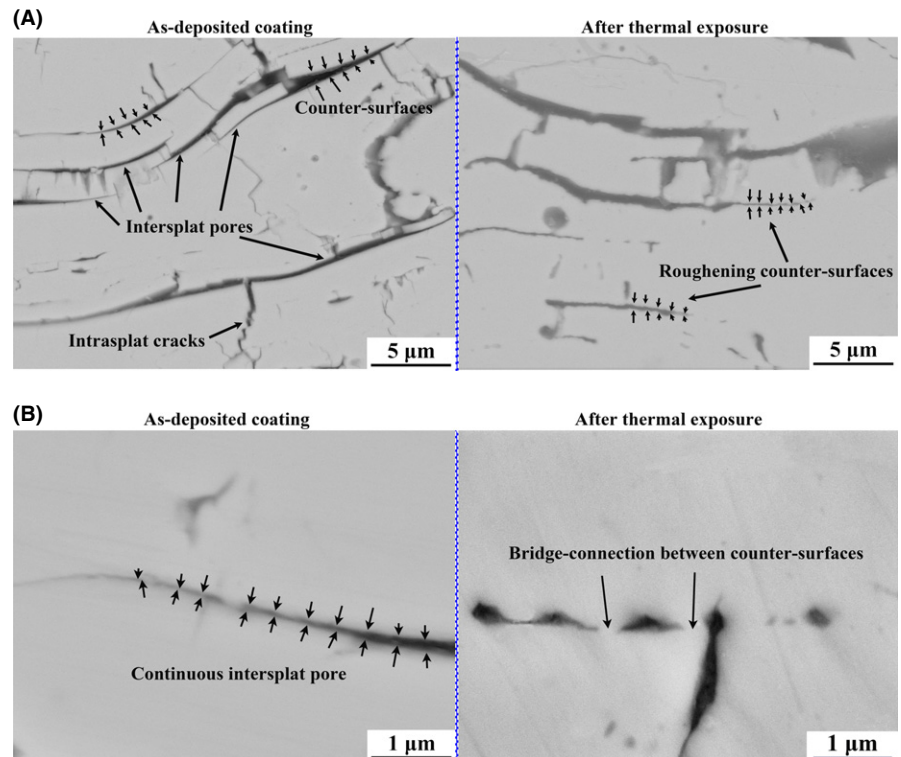


FIGURE 7 Bridge connections between counter-surfaces of intersplat pores after thermal exposure of 10 hours at 1300°C: (A) low magnification and (B) high magnification. The black lines refer to the intersplat pores and intrasplat cracks, and the two edges of the black lines correspond to the counter-surfaces of intersplat pores

4 | DISCUSSION

4.1 | Anisotropic faceting of grain surface and thermal grooving of grain boundaries

The sintering procedure of PS-YSZ coatings is a comprehensive behavior associated with their material and microstructure. To begin with, the intrinsic features corresponding to YSZ material during thermal exposure would be discussed. During thermal exposure, an obvious phenomenon is that the smooth pore surface (splat surface) became roughening at different scales derived from different mechanisms, like the faceting, the thermal grooving and the grain convex. The corresponding roughening heights are approximately 5 nm, 20 nm, and 30 nm, respectively. A schematic diagram of the multiscale roughening induced by thermal exposure at a smooth splat surface can be found in Figure 8. It is worth to address that

this is completely different from the smooth pore surface assumption in reported sintering models.^{9,37-39}

Both the grain-boundary grooving and the surface faceting occur according to thermodynamics. However, the detailed mechanisms are much different. The driving force for the grain-boundary grooving effect can be attributed to the grain-boundary energy, since the decrease of grain-boundary area by the grain-boundary grooving can lead to a decrease in total energy of the system. The effect of grain-boundary grooving can be developed by three mechanisms: evaporation-condensation, surface diffusion, and volume diffusion. These three mechanisms were separately examined by Mullins, while the material was assumed to be of isotropic structure and properties.⁴⁰ After comparing the profiles derived from the three mechanisms, at the temperature of 1000°C-1100°C, the surface diffusion can be regarded as a dominant mechanism leading to the profile of grain-boundary grooving, since this mechanism exhibits

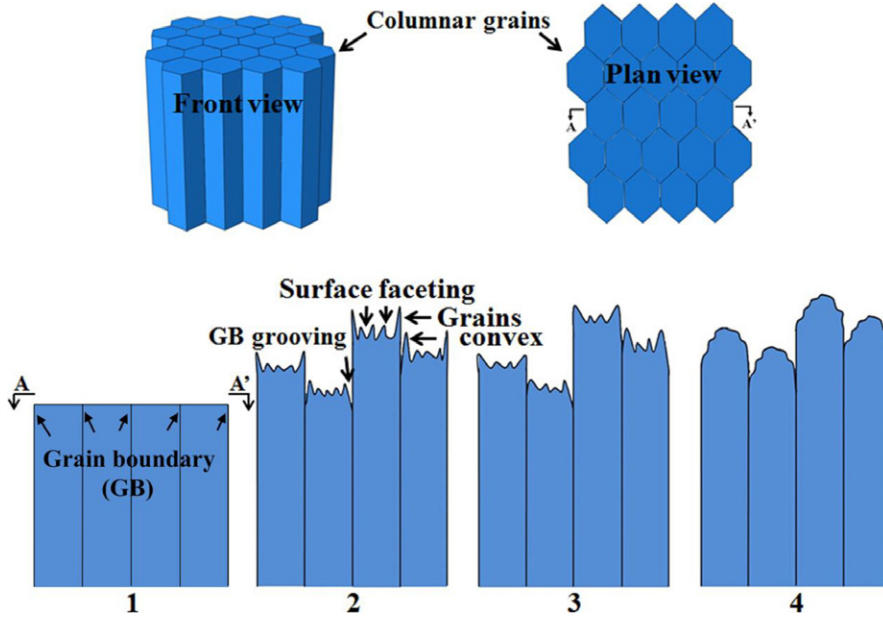


FIGURE 8 Schematic diagram of the multiscale roughening derived from different mechanisms after thermal exposure

both maxima and minima on the groove profile. In contrast, the volume diffusion would act as a dominant one in YSZ at 1300°C as pointed by Trice et al.²²

The surface faceting is due to the anisotropy of specific surface free energy of different crystalline planes. As Mullins made the assumption of isotropy materials, the profile of the groove demonstrates a smoother result. Mass transport by the surface diffusion is driven by the surface Laplacian of curvature. During the grain-grooving process, the isotropy permits that matter always flows from a high curvature domain to a low curvature domain. This theory is conventionally applied in the field of thin metal film used in microelectronics. In this work, it can be employed to explain the faceting in the lamellar structure of TBCs.

According to Mullins' theory, the dominant driving force is the variation of chemical potential, μ_s , which makes atoms migrate from a high-potential position to a low-potential position,

$$\mu_s = \gamma_s K_s \Omega, \quad (1)$$

where K_s is the surface curvature, γ_s is the specific surface free energy, and Ω is the molecular volume. Therefore, the chemical potential can be associated with the curvature.

A relation between the profile of the grooving edge and the time was established in the Cartesian coordinate. Assuming that the x axis is parallel to the surface of a columnar grain, the y axis is along the grain boundary and is set out perpendicular to the free surface. Using the equation $y(x, t)$ to describe the evolution of profile in grain-boundary grooving, where x, y are the Cartesian coordinates and t is the time. A mathematical model describing the evolution of groove shape was developed by Mullins.⁴⁰

$$y(x, t) = m(Bt)^{1/4} \sum_{n=0}^{\infty} a_n \left[\frac{x}{(Bt)^{1/4}} \right]^n \quad (2)$$

where $a_0 = -\frac{1}{\sqrt{2}\Gamma(5/4)}$, $a_1 = 1$, $a_2 = -\frac{1}{2\sqrt{2}\Gamma(3/4)}$, $a_3 = 0$,

$$a_{n+4} = a_n \frac{n-1}{4(n+1)(n+2)(n+3)(n+4)}, \quad (2.1)$$

where m is the slope of the surface at the groove root, and B is the Mullins constant.

The effect of anisotropy by adding a weighting factor to characterize the intensity of anisotropy was reported by Zhang et al.,⁴¹ as described by Equation 3:

$$\mu_s = \left(\gamma_s + \frac{\partial^2 \gamma_s}{\partial \phi^2} \right) K_s \Omega \quad (3)$$

where ϕ is the surface orientation angle, and the term $(\gamma_s + \frac{\partial^2 \gamma_s}{\partial \phi^2})$ is the weighting factor.⁴¹ The other letters have the same meaning as in Equation 1.

Depending on the sign of the weighting factor, the degree of anisotropy is divided into three categories: mild, critical and severe. The mild anisotropy (if the $[\gamma_s + \frac{\partial^2 \gamma_s}{\partial \phi^2}] > 0$ throughout the evolution) demonstrates similar properties as the isotropic materials. The critical anisotropy (if the $[\gamma_s + \frac{\partial^2 \gamma_s}{\partial \phi^2}] \geq 0$ and strict equality holds for some angles ϕ) permits the onset of faceting effect on the grain surface. The severe anisotropy (if the $[\gamma_s + \frac{\partial^2 \gamma_s}{\partial \phi^2}] < 0$ for some ranges of angles ϕ) causes strong faceting effect on the grain surface by transporting the mass from the positions with a low curvature to those with a high curvature.⁴² In this study, the initial evolution of the columnar grain boundary proved the above-mentioned theory and the general results are consistent with the observation by AFM (see Figure 3 and Figure 4). The

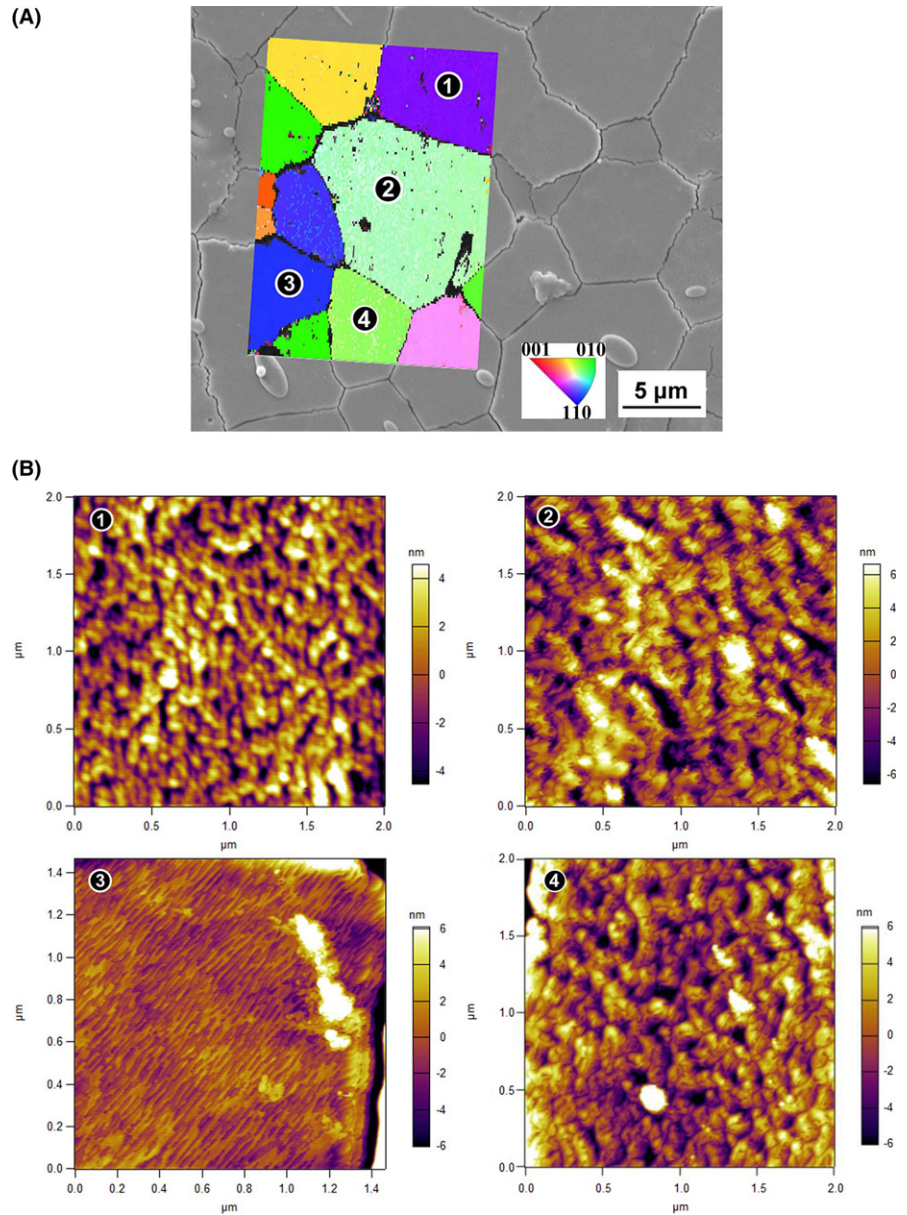


FIGURE 9 Grain orientations (A) and the corresponding surface morphological changes after thermal exposure at 1000°C (B)

grain-grooving effect presents a faceting profile in the surface of grain as the result of anisotropy effect which causes matter flowing from low curvature positions to high curvature positions. However, after the edge of grain having reached a maxima, the effect of anisotropy decreased, as shown in Figure 8, which is quite different from the metallic thin film. This phenomenon indicated that during the evolution of the profile, the weighting factor might change with the increase of annealing time t .

4.2 | Heterogeneous surface morphological changes for different grains on a same splat

In order to correlate the grain lattice orientation and the morphologic changes after thermal exposure, EBSD was used to assist in visualizing the difference of grain lattice

orientations. Figure 9 shows that the original plain grain surfaces with various lattice orientations (which can be determined by EBSD) tend to be roughened in different extents after thermal exposure. Among the four grains shown in Figure 9, grain 2 shows the largest surface faceting, while grain 3 presents the smallest faceting. Moreover, the surface morphological feature of grain 4 was similar to that of grain 2. Correspondingly, the orientations of grain 2 and grain 4 were similar with each other (see Figure 9A). There should be a specific orientation in which the driving force of the anisotropic-specific surface-free energy is the largest and would result in the most remarkable grooving and faceting effects. The orientation distinction also makes the profiles of neighboring grain boundaries to be asymmetric, leading to different convex heights for grains within the same splat. Consequently, the above statistical

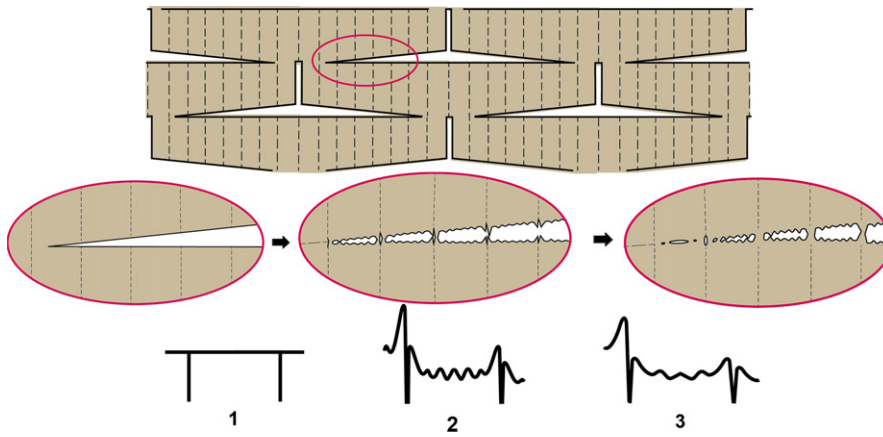


FIGURE 10 Schematic diagram of multiscale multipoint connection enhanced intersplat pore healing at the initial thermal exposure stage

investigation evidently indicates that the different extents of thermal grooving on a same grain surface are attributed to different lattice orientations.

4.3 | Multiscale multipoint connection between lamellar splats

From the structure view of PS-YSZ coatings, as reported in the Part I,¹⁴ the wedge-like morphology of the intersplat pores results in a coexistence of narrow space and wide space. Obvious healing can be found at the narrow tips of the intersplat pores during the initial thermal exposure duration, as shown in Figure 6. This is the dominant sintering behavior at the stage-I.

From the intrinsic-sintering behavior of YSZ material, the discussion above has experimentally and theoretically exhibited that the smooth surface of a splat would be roughening during thermal exposure. This phenomenon stands opposite to the assumption of the typical sintering model⁹ with smooth surface all over the sintering process. Moreover, this multiscale surface roughening is different from the rumpling behavior of thermally growth oxide (TGO) layer observed during thermal exposure.^{43–47} The rumpling of TGO often refers to its undulation growth, which is induced by a compressive stress on the layer. Therefore, the rumpling of TGO often leads to partially debonding due to the morphological change in the whole layer. However, the multiscale roughening in this study just occurs at the surface of splats, owing to the grain boundaries grooving, the surface faceting, as well as the grain growth. Moreover, the whole bulk splat shows relatively little morphological changes. The driving force for the grain-boundary grooving is the decrease in the grain-boundary energy, while the faceting is due to the anisotropy of specific surface-free energy of different crystalline planes. In brief, the basic reason of the multiscale roughening is the sintering-induced matter transport, with the aim to decrease the free energy of the whole system.

As a combination of the microstructure and the material of PS-YSZ coatings, the multiscale roughening of splat

surface may be responsible for the ultrafast healing of wedge-like intersplat pores at the stage-I. The whole sintering process is accompanied with the decrease of free energy of the whole system. To decrease the free energy of the sintering splats, bridging connection seems to be a good choice, as the specific surface energy presents to be much higher than the specific grain-boundary energy. At the narrow space of the intersplat pores, the multiscale roughening induced by thermal exposure leads to multipoint contact of the counter-surfaces, as shown in Figure 10. This process can significantly increase the healing speed of pores instead of a healing from the periphery of a intersplat pore to its center, as reported in previous literatures.^{9,37,38} During the annealing process at a lower temperature (e.g., 1000°C), the surface diffusion is the main mechanism of nondensification,^{9,40} and it promotes the surface of lamellae to groove and facet until the splats next to each other start bridging and connecting. At a higher temperature (e.g., 1300°C), the volume diffusion acts as the main densification factor and it drives the whole coating to shrink in both radial and vertical directions.²²

In brief, the pore boundary healing is induced actually by a multipoint connection, in particular, at the initial sintering stage. This pore boundary healing behavior is completely different from the reported one-dimensional pore healing assumption, which means that the healing proceeds from the periphery of a intersplat pore to its center gradually along its boundary line.^{9,37,38,48} Therefore, this sintering mechanism related to the unique microstructure of PS-YSZ coatings can be responsible for the ultrafast structural and properties evolution at the initial stage of thermal exposure.

5 | CONCLUSIONS

A detailed examination of the interfacial changes between lamellae was carried out to further understand the ultrafast-

sintering kinetics of PS-YSZ coatings when initially exposed. Results show that the dominant structural change at the stage-I was the significant healing of intersplat pores at their tips, which is completely different from the model assumptions reported in previous literatures. To begin with, the pore structure of intersplat pores appears to be wedge-like rather than equally-thick assumed in the reported models. Secondly, different from the smooth surface assumed widely, the as-deposited smooth pore surface became multiscale roughening during thermal exposure. This multiscale roughening of pore surface results from different mechanisms, i.e. grain faceting, grain-boundary grooving, as well as grain undulation. The AFM investigation on individual splats demonstrated the thermal grooving of grain boundary and the faceting effect on inner grain surface during high-temperature exposure. The rate of thermal grooving and faceting changes with different grains in a same splat. EBSD patterns indicate that the lattice orientation of grains in a same splat is different and presents no evident textures. Moreover, the extents of the thermal grooving and the faceting of grain surface are highly associated with the exact orientation of a columnar grain. Thirdly, the multiscale changes of splat surface results in multipoint bridging and connection between lamellae at the wedge-like intersplat pore tips. This is completely different from the assumption of the one-dimensional pore boundary healing made in literatures. Finally, these effects of multipoint connection significantly accelerate the sintering kinetics at the stage-I, which inevitably influences the macroscopic coating properties reported in the Part I. This comprehensive understanding on the sintering behavior of PS-YSZ coatings, in particular, including the extremely fast-sintering kinetics at the initial sintering stage, can contribute greatly to prolonging the service life span of TBCs, and to acting as the working directions for scientists in this field, by reasonably tailoring the microstructure and distribution of these pores in the top coat of TBCs.

ACKNOWLEDGMENTS

The present project was supported by the National Basic Research Program of China (No. 2013CB035701), the Fundamental Research Funds for the Central Universities, and the National Program for Support of Top-notch Young Professionals.

REFERENCES

- Padture NP, Gell M, Jordan EH. Materials science – thermal barrier coatings for gas-turbine engine applications. *Science*. 2002;296:280-284.
- Tian YS, Chen CZ, Wang DY, Ji QM. Recent developments in zirconia thermal barrier coatings. *Surf Rev Lett*. 2005;12:369-378.
- Chi WG, Sampath S, Wang H. Microstructure-thermal conductivity relationships for plasma-sprayed yttria-stabilized zirconia coatings. *J Am Ceram Soc*. 2008;91:2636-2645.
- Yang GJ, Li CX, Hao S, Xing YZ, Yang EJ, Li CJ. Critical bonding temperature for the splat bonding formation during plasma spraying of ceramic materials. *Surf Coat Technol*. 2013;235:841-847.
- Li CJ, Ohmori A. Relationships between the microstructure and properties of thermally sprayed deposits. *J Thermal Spray Technol*. 2002;11:365-374.
- Mcpherson R. On the formation of thermally sprayed alumina coatings. *J Mater Sci*. 1980;15:3141-3149.
- Li GR, Lv BW, Yang GJ, Zhang WX, Li CX, Li CJ. Relationship between lamellar structure and elastic modulus of thermally sprayed thermal barrier coatings with intra-splat cracks. *J Thermal Spray Technol*. 2015;24:1355-1367.
- Paul S, Cipitria A, Tsipas SA, Clyne TW. Sintering characteristics of plasma sprayed zirconia coatings containing different stabilisers. *Surf Coat Technol*. 2009;203:1069-1074.
- Cipitria A, Golosnoy IO, Clyne TW. A sintering model for plasma-sprayed zirconia TBCs. Part I: free-standing coatings. *Acta Mater*. 2009;57:980-992.
- Tan Y, Longtin JP, Sampath S, Wang H. Effect of the starting microstructure on the thermal properties of As-sprayed and thermally exposed plasma-sprayed YSZ coatings. *J Am Ceram Soc*. 2009;92:710-716.
- Thompson JA, Clyne TW. The effect of heat treatment on the stiffness of zirconia top coats in plasma-sprayed TBCs. *Acta Mater*. 2001;49:1565-1575.
- Guo S, Kagawa Y. Young's moduli of zirconia top-coat and thermally grown oxide in a plasma-sprayed thermal barrier coating system. *Scripta Mater*. 2004;50:1401-1406.
- Leigh SH, Lin CK, Berndt CC. Elastic response of thermal spray deposits under indentation tests. *J Am Ceram Soc*. 1997;80:2093-2099.
- Li GR, Xie H, Yang GJ, Liu G, Li CX, Li CJ. A comprehensive sintering mechanism for TBCs-part I: an overall evolution with two-stage kinetics. *J Am Ceram Soc*. DOI: 10.1111/jace.14784, in press. 2017;1-14
- Tsipas SA, Golosnoy IO, Damani R, Clyne TW. The effect of a high thermal gradient on sintering and stiffening in the top coat of a thermal barrier coating system. *J Thermal Spray Technol*. 2004;13:370-376.
- Shaler AJ, Udin H, Kuczynski GC, Bever M. Self-diffusion in sintering of metallic particles- discussion. *Trans Am Inst Min Metall Eng*. 1949;185:896-897.
- Cernuschi F, Bison P, Marinetti S, Campagnoli E. Thermal diffusivity measurement by thermographic technique for the non-destructive integrity assessment of TBCs coupons. *Surf Coat Technol*. 2010;205:498-505.
- Tan Y, Shyam A, Choi WB, Lara-Curzio E, Sampath S. Anisotropic elastic properties of thermal spray coatings determined via resonant ultrasound spectroscopy. *Acta Mater*. 2010;58:5305-5315.
- Dutton R, Wheeler R, Ravichandran KS, An K. Effect of heat treatment on the thermal conductivity of plasma-sprayed thermal barrier coatings. *J Thermal Spray Technol*. 2000;9:204-209.
- Ercan B, Bowman KJ, Trice RW, Wang H, Porter W. Effect of initial powder morphology on thermal and mechanical properties

- of stand-alone plasma-sprayed 7 wt% $\text{Y}_2\text{O}_3\text{-ZrO}_2$ Coatings. *Mater Sci Eng A-Struct.* 2006;435:212-220.
21. Chen DY, Gell M, Jordan EH, Cao E, Ma XQ. Thermal stability of air plasma spray and solution precursor plasma spray thermal barrier coatings. *J Am Ceram Soc.* 2007;90:3160-3166.
 22. Erk KA, Deschaseaux C, Trice RW. Grain-boundary grooving of plasma-sprayed yttria-stabilized zirconia thermal barrier coatings. *J Am Ceram Soc.* 2006;89:1673-1678.
 23. Clarke DR, Oechsner M, Padture NP. Thermal-barrier coatings for more efficient gas-turbine engines. *MRS Bull.* 2012;37:891-902.
 24. Chen X, Wang R, Yao N, Evans AG, Hutchinson JW, Bruce RW. Foreign object damage in a thermal barrier system: mechanisms and simulations. *Mater Sci Eng A-Struct.* 2003;352:221-231.
 25. Sergo V, Clarke DR. Observation of subcritical spall propagation of a thermal barrier coating. *J Am Ceram Soc.* 1998;81:3237-3242.
 26. Richards BT, Begley MR, Wadley HNG. Mechanisms of ytterbium monosilicate/mullite/silicon coating failure during thermal cycling in water vapor. *J Am Ceram Soc.* 2015;98:4066-4075.
 27. Mei H. Thermal shock damage and microstructure evolution of thermal barrier coatings on Mar-M247 superalloy in a combustion gas environment. *Metall Mater Trans A.* 2012;43A:1781-1790.
 28. Kramer S, Yang J, Levi CG, Johnson CA. Thermochemical interaction of thermal barrier coatings with molten $\text{CaO-MgO-Al}_2\text{O}_3\text{-SiO}_2$ (CMAS) deposits. *J Am Ceram Soc.* 2006;89:3167-3175.
 29. Grant KM, Kramer S, Seward GGE, Levi CG. Calcium-magnesium alumino-silicate interaction with yttrium monosilicate environmental barrier coatings. *J Am Ceram Soc.* 2010;93:3504-3511.
 30. Yang GJ, Chen ZL, Li CX, Li CJ. Microstructural and mechanical property evolutions of plasma-sprayed YSZ coating during high-temperature exposure: comparison study between 8YSZ and 20YSZ. *J Thermal Spray Technol.* 2013;22:1294-1302.
 31. Shinmi A, Zhao X, Xiao P. Mechanical and electrical characterization of a phase transformation in thermal barrier coatings. *Surf Coat Technol.* 2010;205:2678-2686.
 32. Ilavsky J, Stalick JK. Phase composition and its changes during annealing of plasma-sprayed YSZ. *Surf Coat Technol.* 2000;127:120-129.
 33. Morterra C, Cerrato G, Ferroni L, Montanaro L. Surface characterization of yttria-stabilized tetragonal ZrO_2 . 1. Structural, morphological, and surface hydration features. *Mater Chem Phys.* 1994;37:243-257.
 34. Thome T, Van LP, Cousty J. Evolution of yttria-stabilized zirconia (100) surface morphology with temperature. *J Eur Ceram Soc.* 2004;24:841-846.
 35. Morrow SL, Luttrell T, Carter A, Batzill M. High temperature scanning tunneling microscopy of purely ion conducting yttria stabilized zirconia (YSZ). *Surf Sci.* 2009;603:L78-L81.
 36. Lahiri J, Mayernick A, Morrow SL, et al. Modification of active sites on YSZ(111) by yttria segregation. *J Phys Chem C.* 2010;114:5990-5996.
 37. Cipitria A, Golosnoy IO, Clyne TW. A sintering model for plasma-sprayed zirconia thermal barrier coatings. Part II: coatings bonded to a rigid substrate. *Acta Mater.* 2009;57:993-1003.
 38. Cipitria A, Golosnoy IO, Clyne TW. Sintering kinetics of plasma-sprayed zirconia TBCs. *J Thermal Spray Technol.* 2007;16:809-815.
 39. Cocks A, Fleck N, Lampenscherf S. A brick model for asperity sintering and creep of APS TBCs. *J Mech Phys Solids.* 2014;63:412-431.
 40. Mullins WW. Theory of thermal grooving. *J Appl Phys.* 1957;28:333-339.
 41. Zhang W, Sachenko P, Gladwell I. Thermal grain boundary grooving with anisotropic surface free energies. *Acta Mater.* 2004;52:107-116.
 42. Zhang W, Gladwell I. Evolution of two-dimensional crystal morphologies by surface diffusion with anisotropic surface free energies. *Comput Mater Sci.* 2003;27:461-470.
 43. Balint DS, Hutchinson JW. An analytical model of rumpling in thermal barrier coatings. *J Mech Phys Solids.* 2005;53:949-973.
 44. Balint DS, Xu T, Hutchinson JW, Evans AG. Influence of bond coat thickness on the cyclic rumpling of thermally grown oxides. *Acta Mater.* 2006;54:1815-1820.
 45. Mei WA, Eric HJB, Gell M. Effect of temperature on rumpling and thermally grown oxide stress in an EB-PVD thermal barrier coating. *Surf Coat Technol.* 2006;201:3289-3298.
 46. Dong H, Yang GJ, Li CX, Luo XT, Li CJ. Effect of TGO thickness on thermal cyclic lifetime and failure mode of plasma-sprayed TBCs. *J Am Ceram Soc.* 2014;97:1226-1232.
 47. Ke PL, Wang QM, Hua WG, Gong J, Sun C, Zhou YC. Stresses and microstructural development of thermal barrier coatings using AIP/D-gun two-step processing. *J Am Ceram Soc.* 2007;90:936-941.
 48. Golosnoy IO, Cipitria A, Clyne TW. Heat transfer through plasma-sprayed thermal barrier coatings in gas turbines: a review of recent work. *J Thermal Spray Technol.* 2009;18:809-821.

How to cite this article: Li G, Xie H, Yang G, Liu G, Li C, Li C. A comprehensive sintering mechanism for TBCs-Part II: Multiscale multipoint interconnection-enhanced initial kinetics. *J Am Ceram Soc.* 2017;00:1-12.
<https://doi.org/10.1111/jace.14940>